

Superconductivity in bulk 2H-MoS_2 via carrier doping

Mingshu Tan(谭明蜀), Helin Mei(梅贺林), Keyi Li(李可意), Wei Ren(任玮), Xueying Ma(马雪英), Shaoshuai Hou(侯少帅), Feng Jin(金峰), Anmin Zhang(张安民), and Qingming Zhang(张清明)
Citation: Chin. Phys. B, 2026, 35 (**5**): 057403. DOI: 10.1088/1674-1056/ae3c93
http://cpb.iphy.ac.cn; http://iopscience.iop.org/cpb

What follows is a list of articles you may be interested in

Intermediately coupled type-II superconductivity in a La-based kagome metal La_3Al

Yingpeng Yu(于英鹏), Zhaolong Liu(刘兆龙), Zhaoxu Chen(陈昭旭), Qi Li(李琦), Yulong Wang(王玉龙), Xuhui Wang(王旭辉), Chunsheng Gong(龚春生), Zhaotong Zhuang(庄照通), Bin-Bin Ruan(阮彬彬), Huifen Ren(任会芬), Peijie Sun(孙培杰), Jian-Gang Guo(郭建刚), and Shifeng Jin(金士锋)
Chin. Phys. B, 2025, 34 (**1**): 017401. DOI: 10.1088/1674-1056/ad8f9f

Superconductivity in kagome metal $ThRu_3Si_2$

Yi Liu(刘艺), Jing Li(厉静), Wu-Zhang Yang(杨武璋), Jia-Yi Lu(卢佳依), Bo-Ya Cao(曹博雅), Hua-Xun Li(李华旬), Wan-Li Chai(柴万力), Si-Qi Wu(武思祺), Bai-Zhuo Li(李佰卓), Yun-Lei Sun(孙云蕾), Wen-He Jiao(焦文鹤), Cao Wang(王操), Xiao-Feng Xu(许晓峰), Zhi Ren(任之), and Guang-Han Cao(曹光旱)
Chin. Phys. B, 2024, 33 (**5**): 057401. DOI: 10.1088/1674-1056/ad1c5e

Superconducting properties of the C15-type Laves phase $ZrIr_2$ with an Ir-based kagome lattice

Qing-Song Yang(杨清松), Bin-Bin Ruan(阮彬彬), Meng-Hu Zhou(周孟虎), Ya-Dong Gu(谷亚东), Ming-Wei Ma(马明伟), Gen-Fu Chen(陈根富), and Zhi-An Ren(任治安)
Chin. Phys. B, 2023, 32 (**1**): 017402. DOI: 10.1088/1674-1056/aca3a2

Growth and characterization of superconducting $Ca_{1-x}Na_xFe_2As_2$ single crystals by NaAs-flux method

Hong-Lin Zhou(周宏霖), Yu-Hao Zhang(张与豪), Yang Li(李阳), Shi-Liang Li(李世亮), Wen-Shan Hong(洪文山), and Hui-Qian Luo(罗会仟)
Chin. Phys. B, 2022, 31 (**11**): 117401. DOI: 10.1088/1674-1056/ac834a

Excess-iron driven spin glass phase in $Fe_{1+y}Te_{1-x}Se_x$

Long Tian(田龙), Panpan Liu(刘盼盼), Tao Hong(洪涛), Tilo Seydel, Xingye Lu(鲁兴业), Huiqian Luo(罗会仟), Shiliang Li(李世亮), and Pengcheng Dai(戴鹏程)
Chin. Phys. B, 2021, 30 (**8**): 087402. DOI: 10.1088/1674-1056/ac0695

RAPID COMMUNICATION

Superconductivity in bulk 2H-MoS_2 via carrier doping

Mingshu Tan(谭明蜀)[1], Helin Mei(梅贺林)[1], Keyi Li(李可意)[1,2], Wei Ren(任玮)[1], Xueying Ma(马雪英)[1], Shaoshuai Hou(侯少帅)[1], Feng Jin(金峰)[2,†], Anmin Zhang(张安民)[1,‡], and Qingming Zhang(张清明)[2,1]

[1] *School of Physical Science and Technology, Key Laboratory of Quantum Theory and Applications of MoE, Lanzhou University, Lanzhou* 730000, *China*
[2] *Beijing National Laboratory for Condensed Matter Physics, Institute of Physics, Chinese Academy of Sciences, Beijing* 100190, *China*

(Received 11 December 2025; revised manuscript received 5 January 2026; accepted manuscript online 23 January 2026)

As a prototypical transition metal dichalcogenide (TMD) semiconductor, MoS_2 exhibits diverse tunable electronic properties in low-dimensional systems, such as Ising superconductivity and charge density waves (CDWs). However, the intrinsic superconductivity of bulk MoS_2 remains underexplored. Here, we demonstrate carrier doping in bulk 2H-MoS_2 using an ionic-liquid-gating method, resulting in anisotropic bulk superconductivity with a critical temperature T_c of 3.2 K. Notably, the superconducting transition in the bulk requires the lowest critical carrier density ($\sim 10^{13}$ cm^{-2}) among all the reported superconducting MoS_2 systems, while exhibiting a higher T_c than typically observed in monolayers. The electron–phonon coupling (EPC) constant extracted from Raman spectroscopy yields a calculated T_c consistent with the experimental observations, in agreement with the mechanism established in monolayer MoS_2. We attribute these observations to the Fermi level preferentially crossing the lower-energy Q point in the bulk, which facilitates superconducting pairing. The results provide deeper insights into the superconducting mechanism in bulk 2H-MoS_2.

Keywords: 2H-MoS_2, bulk superconductivity, ionic liquid, Raman spectroscopy

PACS: 74.70.Xa, 74.62.Dh, 74.25.nd, 74.25.Kc

DOI: 10.1088/1674-1056/ae3c93 **CSTR:** 32038.14.CPB.ae3c93

1. Introduction

Transition metal dichalcogenides, a major class of layered 2D materials following graphene, consist of atomic layers weakly bound by van der Waals forces, enabling dimensional engineering and exhibiting physical properties distinct from their bulk counterparts.[1–5] In 2H-MoS_2, an indirect-to-direct bandgap transition occurs in monolayers,[6,7] making it attractive for bandgap engineering, valleytronics, electronics, and photocatalysis.[8–10] Furthermore, carrier doping in 2H-MoS_2 leads to emergent phenomena such as insulator-to-metal transitions, superconductivity, and CDW order,[11–13] which establish it as one of the most intensively studied TMDs.

In recent years, the superconductivity of MoS_2 has attracted considerable attention. Among various approaches, the electric double-layer gating technique using ionic liquids as dielectrics has been developed to induce high-density surface carriers in monolayer and bilayer samples.[11,14] This electrostatic doping near the K and K' valleys of the conduction band induces superconductivity, resulting in quasi-two-dimensional superconducting states with T_c up to 7–10 K. These states exhibit Ising superconductivity, characterized by upper critical fields that far exceed the Pauli limit.[15–17] In addition, strong electron doping can be achieved via alkali metal intercalation. For instance, in Li-intercalated MoS_2, superconductivity with $T_c \sim 3.7$ K is observed at a carrier density of approximately 10^{15} cm^{-2}. Other alkali ions, such as K^+, tend to induce a coexisting CDW order.[12,18]

Although several studies have reported various tuning strategies for single-crystal MoS_2, investigations into the intrinsic superconducting behavior of bulk 2H-MoS_2 remain scarce. Septianto *et al.* achieved electron doping of single-crystal MoS_2 via K^+ intercalation, leading to the emergence of superconductivity with a T_c of approximately 5 K. However, due to structural modifications induced by intercalation, the superconducting phase appeared in the 1T/1T′ phases.[19] Piatti *et al.* realized strong electron doping in bulk 2H-MoS_2 using organic cations and observed the onset of a strange metallic phase, but no transition to the superconducting state was detected.[20] Pereira *et al.* induced superconductivity in bulk 2H-MoS_2 through TEA^+ intercalation. The significantly enlarged interlayer spacing suggests a dimensional crossover toward a quasi-two-dimensional structure, which likely alters the electronic band structure and implies that the observed superconductivity may originate from monolayer-like characteristics.[21,22]

In this study, we successfully realized a superconducting transition ($T_c = 3.2$ K) in bulk MoS_2 via an ionic-liquid electrochemical method. Structural characterizations indicate that the material retains its intrinsic interlayer coupling. With increasing carrier concentration, the system undergoes a complete sequence from an insulator to a metal and eventually to

†Corresponding author. E-mail: jinfeng@iphy.ac.cn
‡Corresponding author. E-mail: amzhang@lzu.edu.cn

© 2026 Chinese Physical Society and IOP Publishing Ltd. All rights, including for text and data mining, AI training, and similar technologies, are reserved.

a superconductor. We also find that the bulk superconductor requires a significantly lower critical carrier density compared with the monolayers. Moreover, the T_c of bulk superconducting MoS_2 exceeds that of monolayers at comparable carrier densities. Raman measurements reveal an enhancement of EPC with increasing carrier density. We further estimate the EPC constant λ and calculate a T_c that agrees with the experimental value, indicating that superconducting H_x-MoS_2 follows the BCS theory. We propose that, in contrast to monolayer MoS_2 where the Fermi level must first cross the K valley (which does not participate in superconducting pairing), superconductivity in the bulk is triggered when the Fermi level reaches the lower-energy Q point, and dimensionality effects play a critical role in doping-induced changes of T_c.

2. Experiments

High-quality 2H-MoS_2 single crystals were grown by the chemical vapor transport method (provided by Shanghai Pumi Technology Co., Ltd.). The bulk crystals were mechanically exfoliated into uniformly thick flakes with a typical thickness of approximately 20 μm, a dimension chosen to ensure spatial homogeneity during doping. The electrochemical intercalation process for MoS_2 single crystals is schematically illustrated in Fig. 1(a): a MoS_2 flake was mounted on the cathode using indium foil,[23] and a platinum wire coil served as the anode, both immersed in EMIM-TFSI ionic liquid (1-ethyl-3-methylimidazolium bis[(trifluoromethyl)sulfonyl]imide). The doping concentration was systematically tuned by varying the heating temperature, applied bias, and intercalation duration. To investigate the phase transition behavior, all samples were treated at 120 °C, and those doped continuously for 60 h under bias voltages of 3.3 V, 3.6 V, and 4 V were selected for detailed studies. The voltage was limited to 4 V to avoid electrochemical corrosion, which was found to occur at higher biases.

Optical observation and Raman spectra were collected with a LABRAM HR800 system, which is equipped with a single grating of 1800 grooves/mm and a focus length of 800 mm, and liquid-nitrogen-cooled CCD. About 0.1 mW of laser power at 532 nm was focused into a spot with a diameter of ~ 5 μm on the sample surface. Electrical transport and magnetic measurements were performed in a standard four-electrode method using Quantum Design physical property measurement system (PPMS), the lowest temperature and highest magnetic field were 1.8 K and 8 T.

The calculations on the density of electronic states in MoS_2 were preformed via Vienna *ab initio* simulation package (VASP).[24,25] The generalized gradient approximation of the Perdew–Burke–Ernzerhof type[26] was adopted for the exchange–correlation functional. The energy cutoff of the plane-wave basis was set to 380 eV, and a $21 \times 21 \times 4$ k-point mesh for the Brillouin zone sampling was employed. The convergence threshold for energy was 10^{-8} eV and that for force was 0.01 eV/Å.

3. Results and discussion

Figure 1(b) displays the temperature dependence of resistance for samples under different bias voltages. As the voltage increases, the normal-state resistance decreases significantly. At 3.3 V, the sample exhibits semiconducting behavior; at 3.6 V, a transition to a metallic state is observed; and at 4 V, superconductivity emerges. Notably, these electronic phases remain stable even after the removal of the applied bias. To elucidate the relationship between carrier concentration and phase transitions, Hall measurements were performed at 20 K (Fig. 1(c)). The magnitude of the Hall resistance decreases markedly with increasing gate voltage, corresponding to a significant rise in carrier density, which confirms that the continuous phase evolution induced by the electrochemical reaction is governed by electron doping. To probe the microscopic structural and chemical mechanisms responsible for this phenomenon, we characterized the samples before and after doping. As shown in Fig. 1(d), all XRD peak positions remain nearly unchanged after doping, and no intercalation-related peaks are observed. The slight peak broadening observed at 4 V is attributed to local lattice disorder and possible microstrain resulting from the high carrier concentration. This critical finding rules out the possibility of ordered intercalation by the bulky $EMIM^+$ cations. To further identify the actual incorporated chemical species, we conducted detailed chemical analyses (see supplementary material Section A). An approximate atomic ratio of 11 (H^+): 1 ($EMIM^+$) indicates that the intercalation of H^+ (i.e., protonation) from residual water[27] is the absolutely dominant mechanism for electron doping that drives the transition. Hereafter, we refer to these single crystals as H_x-MoS_2. Since H^+ ions diffuse from the edges toward the center of the sample, the doping inevitably introduces some inhomogeneity. To better characterize the superconductivity and evaluate the effect of this non-uniformity, we performed scanning electron microscope and micro-Raman spectroscopy (supplementary material Sections B and C) on different regions, which indicate that there is an acceptably small amount of non-uniformity. Meanwhile, the RRR value of the H_x-MoS_2 is approximately 10, which indicates that our protonated samples have a good crystalline quality. The results demonstrate that such inhomogeneity does not alter the intrinsic physical properties of the material. The room-temperature Raman spectra in Fig. 1(e) reveal that the two characteristic phonon modes, E^1_{2g} and A_{1g}, consistently correspond to the 2H phase structure before and after doping, with no significant change in peak separation. For the 3.3 V sample, the Raman spectrum is indistinguishable from that of the pristine crystal. These results exclude any possibility of dimensional reduction or structural phase transitions.

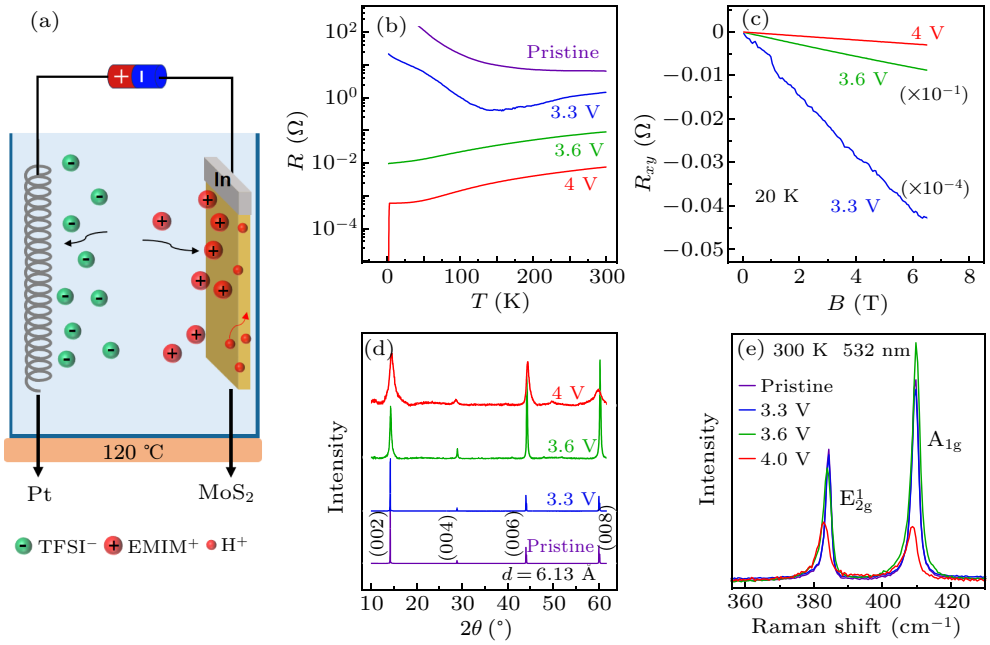


Fig. 1. (a) A schematic diagram of the experimental setup for ionic liquid electrochemical method in bulk MoS_2, the $EMIM^+$ ions are predominantly adsorbed on the surface, whereas the protons generated via ionization processes are incorporated into the sample. (b)–(c) Temperature-dependent resistance at various applied voltages for four samples and the corresponding Hall resistance measurements at 20 K. (d)–(e) XRD patterns and Raman spectra under different bias voltages at room temperature.

We focus on the properties of the superconducting state following the phase transition. As shown in Fig. 2(a), the superconducting H_x-MoS_2 sample obtained under a 4.0 V bias exhibits superconductivity with a T_c of 3.2 K and a sharp single-step transition. The sample retains unchanged superconducting properties including T_c even after three months of air exposure (Fig. 2(a), inset). Furthermore, temperature-dependent magnetic susceptibility measurements were performed to confirm the bulk nature of the superconductivity (see supplementary material Section E for details). Based on Hall effect measurements, we constructed a phase diagram of T_c and the carrier density (n_{2D}) under different doping states as shown in Fig. 2(b). The four superconducting data points were obtained from different H_x-MoS_2 samples at 4.0 V bias and more Hall details see supplementary material Section D. The results show that superconductivity emerges at a carrier density as low as $n_{2D} \sim 1 \times 10^{13}$ cm^{-2}, and T_c remains nearly constant at around 3 K across these samples, with no significant correlation with n_{2D} which contrasts with the typical superconducting dome observed in monolayers and few-layer samples. Comparison with the minimum critical n_{2D} in MoS_2 gated via the electric double layer (EDL) technique reveals that the onset of superconductivity generally requires $n_{2D} > 5 \times 10^{13}$ cm^{-2}, which is significantly higher than the threshold value in bulk superconducting H_x-MoS_2. In other words, superconductivity is more readily achieved in the bulk than in monolayer MoS_2. In addition, within a carrier density range of $n_{2D} \sim 10^{13}$ cm^{-2}, bulk superconducting H_x-MoS_2 exhibits a higher T_c than that of monolayer samples. However, due to the limitation in achievable carrier density, the maximum T_c attainable in the bulk is lower than the highest T_c reported in monolayers. The physical implications of these two features will be further discussed in the following section.

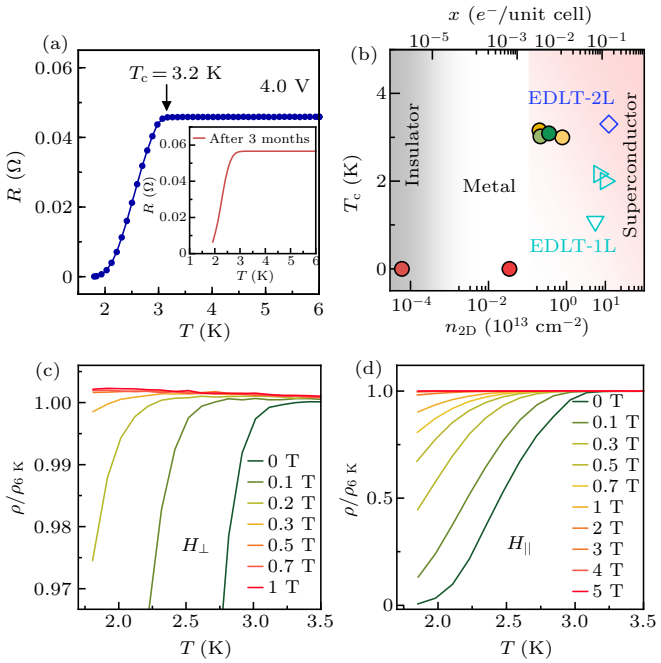


Fig. 2. (a) Superconductivity in bulk H_x-MoS_2, the T_c is defined as the onset temperature T_c^{onset}. (b) Phase diagram of superconductivity in MoS_2 as a function of in-plane carrier density n_{2D} and doping level x, the data from our experiment and EDLT gating. Here, we multiple the bulk carrier density by the monolayer thickness of MoS_2 to obtain the normalized surface carrier density. The solid circles represent experimental data from this work, while the open circles denote results reported for low-dimensional MoS_2 under electrostatic gating, adopted from Refs. [14,16,17]. (c)–(d) Temperature-dependent resistance measurements under application of out-of-plane ($H_\perp$) and in plane ($H_\parallel$) magnetic fields, the upper critical field is determined from the temperature-dependent resistance curves under various magnetic fields at the point where the resistance fully recovers to its normal-state value (100% ρ_n).

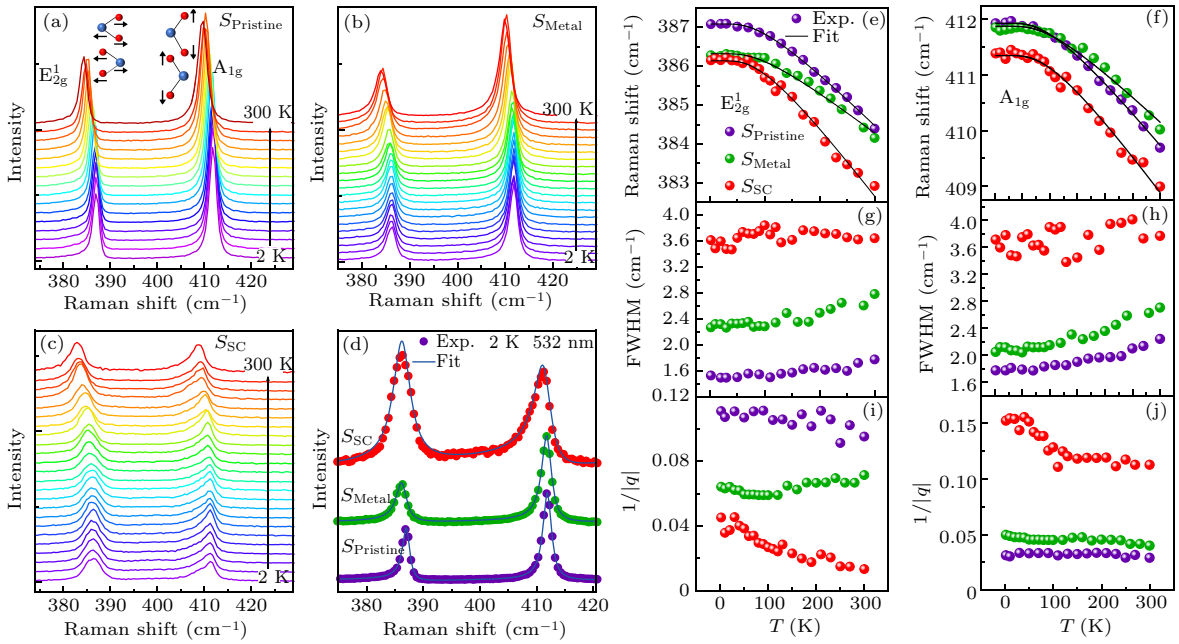


Fig. 3. Raman spectra of MoS_2 at three distinct electronic states. (a)–(c) Temperature-dependent Raman spectra. The sample gated at 3.3 V remains insulating, with Raman spectra showing no changes compared to pristine MoS_2. (d) Raman spectra comparison and Fano fit of the three samples at 2 K. (e)–(j) Temperature dependence of peak positions, linewidths, and Fano asymmetry factors $1/|q|$ of modes E^1_{2g} and A_{1g}. Solid curves correspond to the standard anharmonic fitting.

Figures 2(c) and 2(d) show the temperature dependence of the superconducting transition under magnetic fields applied perpendicular and parallel to the sample plane. From the ratio of out-of-plane ($H^{\parallel}_{c2}$) to in-plane ($H^{\perp}_{c2}$) upper critical fields, we determine an anisotropy parameter $\gamma \approx 8$, indicating significant superconducting anisotropy. Importantly, even for the in-plane direction, the upper critical field remains below the Pauli paramagnetic limit ($H_p \sim 1.86T_c$), which contrasts with the Ising superconductivity observed in monolayer MoS_2. For the TEA^+-intercalated bulk MoS_2, the anisotropy parameter γ is ~ 14, reflecting that significantly expanded interlayer spacing gives rise to monolayer-like behavior.[22] The two-dimensional nature of intercalated MoS_2 has been confirmed by the report.[28] These results indicate that the anisotropy in superconducting H_x-MoS_2 is slightly weaker than that in the monolayer, suggesting that it exhibits quasi-two-dimensional superconductivity.

To further determine the role of electron doping in the superconducting phase transition, we performed variable-temperature Raman scattering experiments. Figures 3(a)–3(c) show the temperature evolution of the two representative Raman-active phonon modes in MoS_2 with different bias voltages: the E^1_{2g} mode (in-plane vibration of Mo atoms) and the A_{1g} mode (out-of-plane vibration of S atoms). For clarity, we refer to the samples obtained under 3.6 V and 4.0 V bias as $S_{\rm Metal}$ (metallic state) and $S_{\rm SC}$ (superconducting state). By comparing Raman spectra, we find that both phonon modes exhibit pronounced asymmetry under different electronic states which is better described by the Fano resonance profile, as shown in Fig. 3(d). The Fano–Breit–Wigner formalism is commonly used to describe the scattering or absorption arising from the interaction between a discrete excitation and a continuum, where the continuum can include multi-phonons, magnons and electrons. Given that our sample is non-magnetic, and that the coupling strength varies with electron doping, the relevant continuum in this case is the electronic continuum. The Fano line shape is described by the following equation:[29,30]

$$I(\omega) = I_0 \frac{(q+\varepsilon)^2}{1+\varepsilon^2}, \quad \varepsilon = \frac{\omega - \omega_0}{\Gamma}, \tag{1}$$

where ω_0 is the bare phonon frequency, Γ is the linewidth parameter associated with the phonon lifetime, and q is the asymmetry parameter. We performed systematic Fano fitting of the E^1_{2g} and A_{1g} phonon modes for the three doping states and extracted the corresponding frequency, linewidth, and asymmetry factor $1/|q|$, as shown in Figs. 3(e)–3(j). As shown in Figs. 3(e) and 3(f), the phonon frequencies in the pristine sample exhibit minimal variation with temperature, indicating weak phonon–phonon interactions. Specifically, the FWHMs of the E^1_{2g} and A_{1g} modes increase by merely 0.24 cm^{-1} and 0.67 cm^{-1} from 1.8 K to 300 K, such temperature-induced changes are slight compared to the significant doping-induced broadening (2 cm^{-1} relative to the pristine sample) observed in the superconducting samples. Upon electron doping, the intrinsic frequencies of the two phonon modes shift markedly relative to the pristine sample, reflecting enhanced EPC. Figures 3(g) and 3(h) display the temperature dependence of the phonon linewidths. In general, the total linewidth Γ of a phonon mode includes contributions from anharmonic decay,

EPC ($\Gamma_{\mathrm{e-ph}}$), and impurity scattering (Γ_{imp}), which can be described by the following equation:

$$\Gamma = \Gamma^{0}_{\mathrm{anh}}\left(1+\frac{2}{e^{\hbar\omega_0/2k_{\mathrm{B}}T}-1}\right) + \Gamma_{\mathrm{e-ph}} + \Gamma_{\mathrm{imp}} + \Gamma', \tag{2}$$

where $\Gamma^{0}_{\mathrm{anh}}$ is the anharmonic linewidth at 0 K, Γ' represents the additional scattering term induced by carrier injection. The linewidths in the MoS_2 system exhibit only slight changes with temperature, showing that the intrinsic Γ_{anh} and Γ_{imp} contributions are very weak. Therefore, the massive linewidth broadening observed in the superconducting state relative to the pristine MoS_2 is primarily attributed to the emergence of $\Gamma_{\mathrm{e-ph}}$ and Γ'. Critically, our XRD analysis confirms the presence of significant doping-induced disorder via peak broadening (meaning the Γ' term is substantial). Given this contribution from Γ', and that both phonon modes exhibit comparably large linewidths, it becomes impractical to quantitatively de-convolute the specific $\Gamma_{\mathrm{e-ph}}$ contribution from the total measured broadening. However, in the metallic state, the E^{1}_{2g} mode exhibits a more pronounced linewidth broadening compared to the A_{1g} mode. The linewidth broadening in the metallic state also originates from $\Gamma' + \Gamma_{\mathrm{e-ph}}$. Given the similar phonon energies of the E^{1}_{2g} and A_{1g} modes, we further assume that they have the same Γ'. Based on these, we further extract the contribution of $\Delta\Gamma_{\mathrm{e-ph}}$ between the E^{1}_{2g} and A_{1g} modes to be 0.2547 cm^{-1}. As shown in Figs. 3(i) and 3(j) the q values reveal pronounced changes in the asymmetry of both the E^{1}_{2g} and A_{1g} phonon modes. These results indicate a significant enhancement of the EPC with increasing carrier concentration.

To check the role of EPC in superconducting H_x-MoS_2, we have estimated the EPC constant λ in the superconducting state using the Allen formula based on the intrinsic phonon linewidth,[31–33] which is expressed as

$$\lambda = \frac{\Gamma_{\mathrm{e-ph}}}{\pi N(E_{\mathrm{F}})\omega_0^2}, \tag{3}$$

where $N(E_{\mathrm{F}})$ is the bare density of states at the Fermi level. We therefore calculate the DOS using the carrier density derived from band filling with estimate $N(E_{\mathrm{F}}) = 0.1742$ states/eV/spin/unit cell from Fig. 4(a). Based on the above analysis, we assume $\Gamma^{A_{1g}}_{\mathrm{e-ph}} \approx 0$, leading to $\Gamma^{E^{1}_{2g}}_{\mathrm{e-ph}} = \Delta\Gamma_{\mathrm{e-ph}} = 0.2547$ cm^{-1}. We obtain $\lambda_i = 0.0251$ for the E^{1}_{2g} mode, considering that all 18 modes in MoS_2 contribute equally to the total EPC, we estimate $\lambda_{\mathrm{total}} = 0.453$. However, the resulting value should be regarded as a lower bound or reference estimate rather than a precise quantitative result. This is because the EPC-induced linewidth of the E^{1}_{2g} mode obtained via this method corresponds to the difference between the EPC contributions of the E^{1}_{2g} and A_{1g} modes — an approach that inherently leads to an underestimation of the total EPC for the E^{1}_{2g} mode. Within the BCS framework, the T_{c} can be estimated by the Allen–Dynes modified McMillan equation[31,32,34,35]

$$T_{\mathrm{c}} = \frac{\omega_{\log}}{1.20}\exp\left(-\frac{1.04(1+\lambda)}{\lambda-\mu^{*}(1+0.62\lambda)}\right), \tag{4}$$

where μ^{*} is the Coulomb pseudopotential parameter, typically taken as 0.1 for bulk systems, $\omega_{\log}$ is 384 K.[36] This yields a T_{c} of approximately 3.05 K for the metallic state, which is consistent with the experimental result in the superconducting sample and will be discussed in detail below.

In both the metallic and superconducting states, the EPC matrix elements remain unchanged due to the identical phonon and electronic structure. Meanwhile, the quasi-two-dimensional nature of the energy bands near the Q point ensures that the density of states at the Fermi level is the same in both states (see supplementary material Section F for details). According to BCS theory, this would imply the same T_{c}. However, unlike in 3D systems, 2D systems are characterized by distinct pairing and phase coherence temperatures (T_{coh}). Our estimated T_{c} corresponds to the pairing temperature, while the experimentally observed critical temperature T_{c} is determined by the lower of these two scales.[37,38] While the pairing temperature is independent of carrier concentration, the T_{coh} increases linearly with doping.[39] As a result, the lower carrier concentration in the metallic state leads to a T_{coh} that is approximately 1/3 of that in the superconducting state, rendering the superconducting transition unobservable in the metallic regime. When T_{coh} exceeds the pairing temperature, T_{c} is determined by the latter, which explains the nearly constant critical temperature observed across different doping levels in Fig. 2(b).

We now address why the critical carrier density required to induce superconductivity in bulk MoS_2 is nearly an order of magnitude lower than that in monolayers. As shown in Fig. 4(b), with increasing layer stacking, the conduction bands at both the K and Q symmetry points shift downward-with the Q-point band decreasing more rapidly and eventually becoming the global conduction band minimum. This band reordering leads to a transition from a direct-gap to an indirect-gap semiconductor, as illustrated in Fig. 4(a). In monolayer and few-layer systems, Piatti *et al.*[16] established that injected carriers initially populate the lower-energy K valley, and superconductivity emerges only after the carrier density reaches a critical value ($\sim 1\times10^{14}$ cm^{-2}), corresponding to the onset of Q-valley occupation. This observation confirms the Q valley as the primary source of superconducting carriers. In contrast, in bulk crystals, the lowered energy of the Q valley leads to its preferential filling, thereby enabling superconductivity at a substantially lower carrier density ($\sim 1\times10^{13}$ cm^{-2}). Thus,

the Q-valley universally governs superconductivity across dimensionalities. In addition, the enhanced T_c in bulk materials is further attributed to stronger Coulomb screening relative to monolayers, which reduces the effective μ^* and consequently raises T_c. Notably, whereas monolayer Ising superconductivity requires simultaneous occupation of both the Q_1 and Q_2 bands, the bulk system exhibits superconductivity with only the Q_1 band being populated, as supported by the carrier density and DOS analysis in Fig. 4(a). This dimensional contrast is likely due to strong spin–orbit coupling in monolayers and thus warrants further investigation.

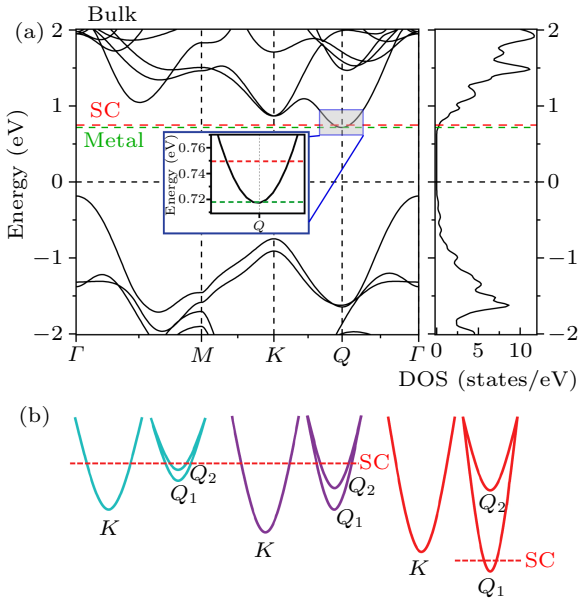


Fig. 4. (a) Band structure and DOS of bulk H_x-MoS_2, the green and red dashed lines mark the electron occupation locations in the metallic and superconducting states, respectively. (b) Band evolution at the K and Q points as a function of dimensionality.

4. Conclusion

In summary, we successfully achieved protonation in bulk MoS_2 via ionic-liquid electrochemical method, driving phase evolution from the semiconducting to the metallic and eventually to the superconducting state. We estimated the T_c within the BCS framework using the EPC constant λ extracted from variable-temperature Raman measurements. The calculated T_c agrees with the experimental value, supporting the conclusion that superconductivity in this system is mediated by electronphonon coupling. Compared with monolayer samples, the bulk exhibits both a lower critical carrier density required for superconductivity and a higher T_c, we provide an interpretation of these behaviors based on the electronic band structure. We find that although both bulk and monolayer superconductivity emerge at the Q valley, the bulk system only requires occupation of the lower Q_1 band, in contrast to the monolayer case. This distinction may explain why bulk superconductivity does not exhibit Ising pairing behavior. Our work elucidates the superconducting mechanism in bulk MoS_2 and opens up new possibilities for developing other bulk 2H-phase TMDs in electronic modulation and device applications.

Acknowledgements

This work was supported by the National Key Research and Development Program of China (Grant Nos. 2024YFA1408300 and 2022YFA1402704), the National Science Foundation of China (Grant No. 12274186), the Strategic Priority Research Program of the Chinese Academy of Sciences (Grant No. XDB33010100), and the Synergetic Extreme Condition User Facility (SECUF, https://cstr.cn/31123.02.SECUF). The authors acknowledge the support provided by the Supercomputing Center of Lanzhou University and the high-level talents funding of Lanzhou.

References

[1] Novoselov K S, Geim A K, Morozov S V, Jiang D, Katsnelson M I, Grigorieva I V, Dubonos S V and Firsov A A 2005 *Nature* **438** 197
[2] Zhang Y, Tan Y W, Stormer H L and Kim P 2005 *Nature* **438** 201
[3] Novoselov K S, Geim A K, Morozov S V, Jiang D, Zhang Y, Dubonos S V, Grigorieva I V and Firsov A A 2004 *Science*
[4] Geim A K and Grigorieva I V 2013 *Nature* **499** 419
[5] Yan B and Felser C 2017 *Annual Review of Condensed Matter Physics* **8** 337
[6] Mak K F, Lee C, Hone J, Shan J and Heinz T F 2010 *Phys. Rev. Lett.* **105** 136805
[7] Kuc A, Zibouche N and Heine T 2011 *Phys. Rev. B* **83** 245213
[8] López-Suárez M, Neri I and Rurali R 2016 *J. Appl. Phys.* **119** 165105
[9] Zeng H, Dai J, Yao W, Xiao D and Cui X 2012 *Nat. Nanotech.* **7** 490
[10] Fathipour S, Remskar M, Varlec A, Ajoy A, Yan R, Vishwanath S, Rouvimov S, Hwang W S, Xing H G, Jena D and Seabaugh A 2015 *Appl. Phys. Lett.* **106** 022114
[11] Ye J T, Zhang Y J, Akashi R, Bahramy M S, Arita R and Iwasa Y 2012 *Science* **338** 1193
[12] Bin Subhan M K, Suleman A, Moore G, Phu P, Hoesch M, Kurebayashi H, Howard C A and Schofield S R 2021 *Nano Lett.* **21** 5516
[13] Rösner M, Haas S and Wehling T O 2014 *Phys. Rev. B* **90** 245105
[14] Saito Y, Nojima T and Iwasa Y 2016 *Supercond. Sci. Technol.* **29** 093001
[15] Saito Y, Nakamura Y, Bahramy M S, Kohama Y, Ye J, Kasahara Y, Nakagawa Y, Onga M, Tokunaga M, Nojima T, Yanase Y and Iwasa Y 2016 *Nat. Phys.* **12** 144
[16] Piatti E, De Fazio D, Daghero D, Tamalampudi S R, Yoon D, Ferrari A C and Gonnelli R S 2018 *Nano Lett.* **18** 4821
[17] Fu Y, Liu E, Yuan H, Tang P, Lian B, Xu G, Zeng J, Chen Z, Wang Y, Zhou W, Xu K, Gao A, Pan C, Wang M, Wang B, Zhang S C, Cui Y, Hwang H Y and Miao F 2017 *npj Quant. Mater.* **2** 1
[18] Piatti E, Chen Q and Ye J 2017 *Appl. Phys. Lett.* **111** 013106
[19] Septianto R D, Romagosa A P, Dong Y, Matsuoka H, Ideue T, Majima Y and Iwasa Y 2024 *Nano Lett.* **24** 13790
[20] Piatti E, Montagna Bozzone J and Daghero D 2022 *Nanomaterials* **12** 1842
[21] Tan M, Mei H, Liao Z, Ma X, Li K, Ren W, Hou S, Ji J, Jin F, Yu Z, Zhang J, Qiu X, Zhang A and Zhang Q 2025 *Phys. Rev. B* **111** 195119
[22] Pereira J M, Tezze D, Niehues I, Asensio Y, Yang H, Mester L, Chen S, Casanova F, Bittner A M, Ormaza M, Schiller F, Martín-García B, Hillenbrand R, Hueso L E and Gobbi M 2022 *Adv Funct. Mater.* **32** 2208761
[23] Shi M, Kang B, Wu T and Chen X 2022 *Chin. Phys. B* **31** 107403
[24] Kresse G 1996 *Phys. Rev. B* **54** 11169
[25] Kresse G and Furthmüller J 1996 *Comput. Mater. Sci.* **6** 15
[26] Perdew J P 1996 *Phys. Rev. Lett.* **77** 3865

[27] Lu N P, Zhang P F, Zhang Q H, *et al.* 2017 *Nature* **546** 124
[28] Jo M K, Lee E, Moon E, Jang B G, Kim J, Dhakal K P, Oh S, Cho S R, Hasanah N, Yang S, Jeong H Y, Kim J, Kang K and Song S 2024 *Adv. Mater.* **36** 2407997
[29] Fano U 1961 *Phys. Rev.* **124** 1866
[30] Abstreiter G, Cardona M and Pinczuk A 1984 *Light scattering by free carrier excitations in semiconductors* (Berlin, Heidelberg: Springer) pp. 5–150
[31] Allen P B 1974 *Solid State Commun.* **14** 937
[32] Allen P B 1972 *Phys. Rev. B* **6** 2577
[33] Rowan L G 1968 *Phys. Rev.* **167** 326
[34] Allen P B and Dynes R C 1975 *Phys. Rev. B* **12** 905
[35] Ren W, Mei H, Sang W, Tan M, Si J, Liu M, Ji J, Jin F, Zhang A and Zhang Q 2024 *Phys. Rev. B* **110** 144504
[36] Hromadová L, Martoňák R and Tosatti E 2013 *Phys. Rev. B* **87** 144105
[37] Sharma C H, Surendran A P, Varma S S and Thalakulam M 2018 *Commun. Phys.* **1** 90
[38] Jarjour A, Ferguson G M, Schaefer B T, Lee M, Loh Y L, Trivedi N and Nowack K C 2023 *Nat. Commun.* **14** 2055
[39] Kosterlitz J M and Thouless D J 1973 *J. Phys. C: Solid State Phys.* **6** 1181